

RESEARCH ARTICLE

10.1002/2016JB012833

Key Points:

- A middle to lower crust density anomaly coincides with the Sengan volcano cluster and is consistent with a hot zone magma intrusion model
- Axisymmetric numerical models confirm dynamic uplift of the crust across volcanic clusters

Supporting Information:

- Supporting Information S1

Correspondence to:

O. A. George,
oageorge@mail.usf.edu

Citation:

George, O. A., R. Malservisi, R. Govers, C. B. Connor, and L. J. Connor (2016), Is uplift of volcano clusters in the Tohoku Volcanic Arc, Japan, driven by magma accumulation in hot zones? A geodynamic modeling study, *J. Geophys. Res. Solid Earth*, 121, 4780–4796, doi:10.1002/2016JB012833.

Received 19 JAN 2016

Accepted 5 JUN 2016

Accepted article online 10 JUN 2016

Published online 28 JUN 2016

Is uplift of volcano clusters in the Tohoku Volcanic Arc, Japan, driven by magma accumulation in hot zones? A geodynamic modeling study

Ophelia A. George¹, Rocco Malservisi¹, Rob Govers², Charles B. Connor¹, and Laura J. Connor¹

¹School of Geosciences, University of South Florida, Tampa, Florida, USA, ²Department of Earth Sciences, Utrecht University, Utrecht, Netherlands

Abstract In many volcanic arcs, the rate of tectonic uplift cannot be explained by lithospheric plate motion alone but may be associated with dynamic uplift. Buoyant forces associated with underplated magma bodies lift the upper crust and leads to relatively high rates of topographic change. One such region is northern Honshu, Japan, where Quaternary volcano clusters are spatially associated with uplifted crust and isostatic gravity anomalies. Axisymmetric inversion of Bouguer gravity data for the Sengan volcano cluster shows that these gravity anomalies can be modeled by 30 km radius bodies emplaced at ~15 km depth. Axisymmetric, finite element models, generated using GTECTON, of a layered Earth representative of the Tohoku crust indicate that the deformation of these midcrustal intrusions produces elevated topography on the surface directly above the intrusion that is bounded by a shallow peripheral trough. The wavelengths of vertical deformation produced by these bodies are sensitive to the thickness of the models' elastic layer and relatively insensitive to the models' rheology. This suggests that the amplitude of the vertical deformation represents a trade-off between the size of the intrusion and the thickness of the elastic layer and is less strongly influenced by the rheology of the lithosphere into which the bodies are emplaced. Our results are consistent with hot zone and hot finger models for the arc and indicate that Tohoku Volcanic Arc features such as gravity anomalies and uplifted basement are related to crustal magma intrusions and hot zones rather than directly related to mantle processes.

1. Introduction

Volcanism and associated magmatic processes can result in significant regional uplift by vertical deformation above shallow intrusions. Stresses induced by the intrusion of buoyant magma into the lower and middle crust may also provide dynamic support of topography and induce regional uplift [Tizzani *et al.*, 2009; Fialko and Pearce, 2012]. Surface exposures of young batholiths, such as the Takidani Granodiorite (intruded 2.4 Ma and exposed 0.7 Ma) [Harayama, 1992] and the Yugura-dake quartz diorite (emplaced 1.2 Ma) [Kurasawa *et al.*, 1989], indicate that the emplacement and unroofing of intrusive magmatic bodies has taken place during the Quaternary within Tohoku Volcanic Arc (TVA), northern Honshu Island, Japan. These observations could be explained by relatively low-density magma at the crust-mantle boundary (Moho) or within the crust, producing isostatic adjustments or local uplift in response to the change in bulk density of the crust. Theoretically, the accumulation of large volumes of magma might be associated with negative long-wavelength gravity anomalies due to the contrast between the low-density magma and the surrounding mantle or crustal rock [Bott, 1953; Rymer and Brown, 1986; Walker, 1989; Singh *et al.*, 2014].

1.1. Volcano Clusters and Their Association With Mantle Hot Fingers

Regional gravity observations made in northern Honshu do show numerous negative Bouguer gravity anomalies that are closely associated with, and in some cases coincide with, clusters of Quaternary volcanoes [Tamura *et al.*, 2001, 2002]. These volcano clusters are 30–50 km in diameter, with trench-parallel gaps in volcanic activity of approximately 70 km, separating each cluster [Mahony *et al.*, 2009]. Tamura *et al.* [2002] found that the basement beneath each volcano cluster is topographically elevated by more than 500 m with respect to the basement elevations in the gaps between volcano clusters. Along the TVA are a series of dipping low-velocity seismic zones within the asthenospheric wedge parallel to the direction and dip of plate subduction [Zhao *et al.*, 1990; Hasegawa *et al.*, 1993, 2013; Xia *et al.*, 2007]. These low-velocity zones are thought to result from ascending flow of hot mantle material associated with the influx of fluids from the

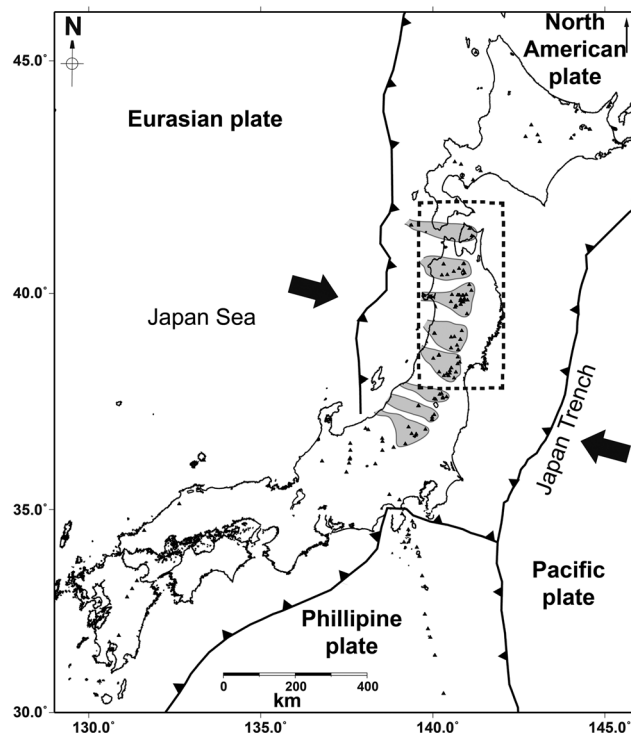


Figure 1. Map of Japan showing the location of the trenches and the Quaternary volcanic vents of the Tohoku Volcanic Arc (TVA) (region outlined by the dashed black box) as well as the location of other Quaternary vents distributed throughout the Japanese Islands. Subduction of the Pacific plate beneath the North America plate occurs at a rate of about 8–10 cm/yr in the region of Tohoku. Quaternary volcanic centers are represented by the black triangles; the direction of plate motion is indicated by the heavy black arrows. The locations of mantle “hot fingers” proposed by *Tamura et al.* [2002] are indicated by the grey shading.

down-going slab [*Wang and Zhao, 2005*]. Partial melting of the mantle and overlying crust is marked by areas where these low-velocity zones extend upward to the Moho and sometimes appear to penetrate the crust on tomographic images.

Combining the observation of locally elevated topography with seismic tomography models and gravity data, *Tamura et al.* [2002] suggested the presence of “hot fingers” within the asthenosphere. The hot fingers and associated shallower low-velocity zones are spaced at 10–70 km along the TVA [*Tamura et al., 2002*] and coincide with clusters of Quaternary volcanoes mapped in the arc [*Kondo, 2009*] (Figure 1). Thus, volcanism in the TVA is characterized by trench-perpendicular variations in magma productivity, as explained by 2-D subduction zone models [*Pearce and Peate, 1995*], and substantial trench-parallel variations in magma productivity, thought to originate from the complexity of circulation in the asthenospheric wedge, the development of hot fingers, and the increased flux of magma into the crust that results. Several 2-D and 3-D numerical simulations of mantle wedge flow dynamics have revealed the development of small-scale convection cells (SSC) within the mantle wedge that share many similarities to the proposed “hot fingers” in the TVA [*Honda and Saito, 2003; Honda et al., 2010; Davies et al., 2016*]. The simulated cells were found to develop in models of hydrated mantle as gravitational instabilities at the base of the overriding plate; longitudinal SSCs were parallel to the direction of plate motion (i.e., their axes are perpendicular to the trench) and were of similar extents to the proposed hot fingers (100 km long and at least 50 km wide). These SSCs were found to be stable for about 1–5 Myr in the subarc region and 5–10 Myr in the back-arc region. Comparison of low seismic velocities from the *Zhao et al.* [1994] study with those calculated from laboratory data for partial melting experiments on dry solid and molten peridotites, basalt melts, and molten hydrous peridotites with 1 and 2 wt % water by *Sato et al.* [1999] indicated that these velocities correspond to temperatures of 1200°C and 1100–1300°C at depths of 40 and 80 km depths, respectively. The hot fingers may therefore represent SSCs formed by the interaction of liberated slab fluids with the mantle wedge and may be the source region of arc magmas. *Tamura et al.* [2002] concluded that in the long term, the development of these hot fingers within the asthenospheric

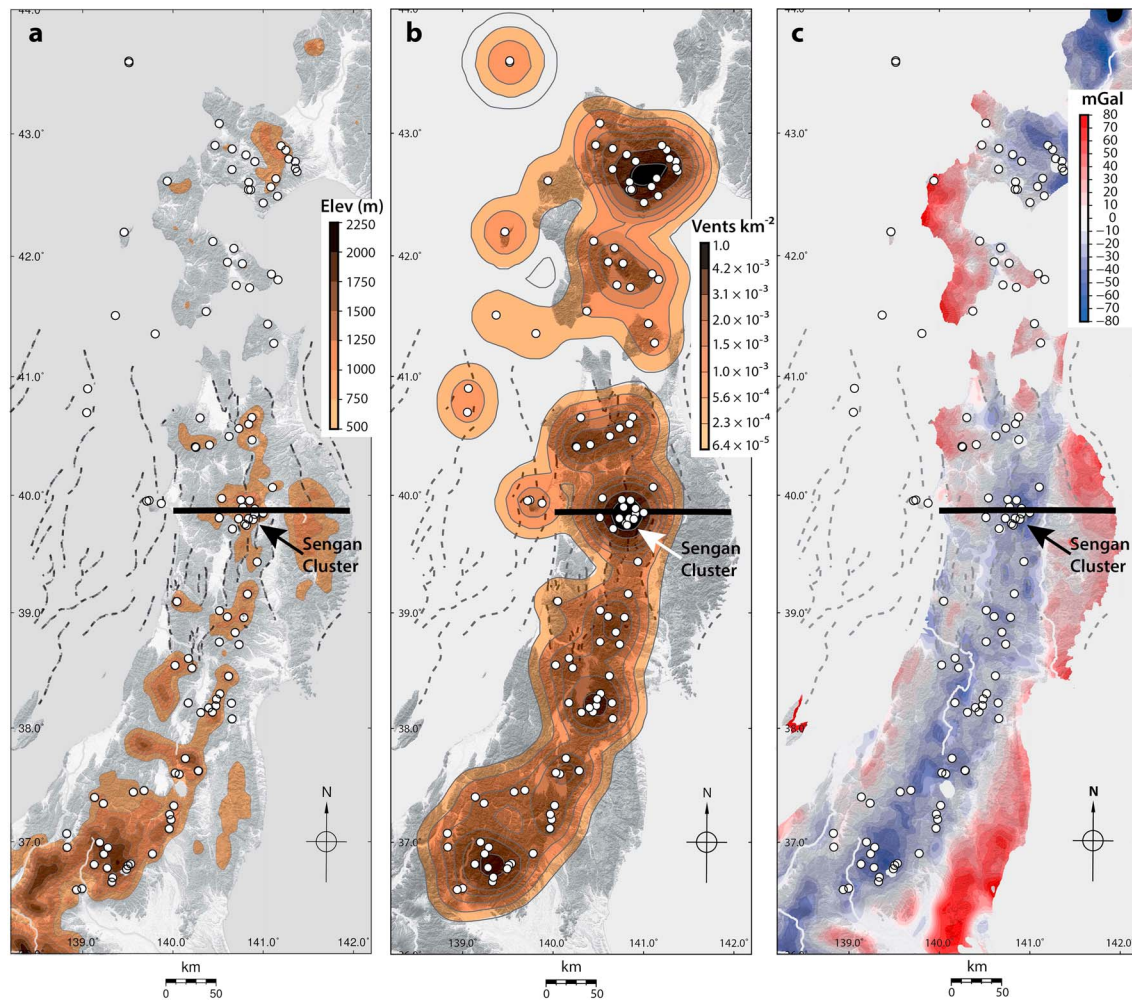


Figure 2. (a) Shaded relief map of the TVA which is overlain (brown) by the same DEM data low-pass filtered at 20 km emphasizes the variation in topography associated with many of the volcanic clusters. (b) Spatial intensity map of the Quaternary volcanoes in the TVA shows that the location of the highest number of vents/unit area coincides with both the location of topographic highs (map a) and gravity lows (map c). (c) Map of Bouguer anomalies for the Tohoku region low-pass filtered using a Gaussian filter with a half weight at 10 km, detrended to remove the signal due to the subducting slab and contoured in 10 mGal intervals. From this map it can be seen that the volcanic centers primarily occur in areas of relatively low Bouguer anomalies. The solid black line drawn on this map indicates the location of the observed gravity profile used in the inversion described in Figure 4. Gravity map was produced from regional gravity data compiled by the Geological Survey of Japan [Komazawa *et al.*, 2004]. White circles indicate the location of Quaternary vents, and active faults are shown as dashed lines.

wedge is reflected in clustered volcano distribution at the surface and provides a buoyant driving force that creates localized bending of the crust.

1.2. Crustal Hot Zones

Although Tamura *et al.*'s [2002] scenario provides a valuable correlation between the tomographic data and the size and spacing of volcano clusters, the wavelengths of the Bouguer gravity anomalies and the topographic basement (locally elevated terrain atop which the volcanoes sit) are much shorter than expected to result directly from an asthenospheric wedge process. For asthenospheric features as extensive as the hot fingers appear to be, the corresponding gravity anomalies should have wavelengths on the order of 200 km or greater, as opposed to ~50 km observed in the TVA (see Figure 2c). One way to account for this discrepancy is to associate hot fingers in the asthenospheric wedge with hot zones in the lower and middle crust [Annen *et al.*, 2006, 2015]. In the hot zone model by Annen *et al.* [2006], primary mafic magmas are emplaced as discrete sills at depths of 30 km or greater within the crust or at the Moho. Continued release of heat from the crystallizing sills, which are repeatedly emplaced in the crust over time, leads to the development of a region of elevated temperatures (i.e., the hot zone). Melts eventually segregate out of these sills and ascend to the shallow level magma chambers due to compaction and the buoyancy contrast between the melt and the host

rock. The presence of these hot zones within the Tohoku crust and their close association with asthenospheric “hot fingers” is supported by low-velocity regions at depths of about 30 km (Moho) in the tomographic images presented by *Zhao et al.* [1992, 1994]; higher-resolution tomographic studies by *Hasegawa et al.* [1993, 2013] indicate the existence of low-velocity zones within the crust beneath active volcanoes extending from the Moho to about 7 km. These low-velocity features in the crust along with their associated low-velocity mantle upwelling zones extend throughout the entire length of the arc [*Hasegawa et al.*, 2013] and may be a common subduction zone feature. For instance, similar low-velocity features have been imaged beneath the Central Andean Volcanic arc [*Schurr et al.*, 2003].

In this paper, we investigate the expected dynamic support and uplift associated with hot zones. Our goal is to explain the comparatively short wavelengths of gravity anomalies, topographic uplift, and volcano clusters in the TVA, which cannot be explained by asthenospheric processes alone. We consider that magmatic hot zones developed below the Moho (~30 km depth) and within the midcrust below the Conrad density discontinuity (~15 km depth). We estimate expected dynamic adjustments and expected gravity anomalies using axisymmetric finite element models in which hot zones are approximated as circular disks of varying diameter, thickness, and bulk density. In addition to the effects of the hot zone size and volume, we test the effects of elastic layer thickness and crustal rheological properties on expected uplift rates. By monitoring model sensitivity to these different parameters, we can test the hypothesis that the wavelengths and amplitudes of topographic and gravity signals associated with volcano clusters in the TVA may be explained by hot zones in the middle or lower crust.

2. Model Setup

2.1. Model Development

To design models that are an accurate representation of the TVA, we examine two sources of data. First, we explore the distribution of Quaternary volcanoes in the TVA in concert with simple processing of Bouguer gravity data over the same region. Second, we conduct axisymmetric inversions of the gravity data to find suitable intrusion geometries and density contrasts for the problem at hand.

2.1.1. Distribution of Quaternary Volcanoes in the TVA

The catalog of Quaternary volcanoes of the TVA contains a total of 120 volcanoes known to have erupted during the last 2 Ma [*Nakano et al.*, 2013]. Most of these volcanoes are composite volcanoes and volcanic systems, but the arc includes a large number of calderas, maars, and lava domes. Many authors have noted that volcanoes tend to cluster within the TVA, and the most prominent of these clusters is the Sengan cluster [*Martin et al.*, 2004; *Ueki and Iwamori*, 2007; *Kulatilake et al.*, 2007; *Mahony et al.*, 2009], consisting of approximately 28 Quaternary volcanoes (Figure 2a). A map of spatial intensity (volcanoes per square kilometer), generated from the catalog of Quaternary volcanoes, illustrates the clustered nature of TVA volcanism (Figure 2b). This spatial intensity map is constructed using an isotropic Gaussian kernel density function, with kernel bandwidth estimated from the volcano distribution using a smoothed asymptotic mean-square error algorithm [*Connor and Connor*, 2009; *Connor et al.*, 2015]. One standard deviation of the best fit isotropic Gaussian kernel is approximately 52 km.

The spatial intensity map reveals the clusters discussed by *Tamura et al.* [2002] and highlights the prominence of the Sengan cluster. A similar study by *Martin et al.* [2004] showed that when these mapped volcano clusters are grouped into 10 km² bins, more than 70 % of the vents occur in regions with *P* wave velocity perturbations of –2%, and 10% fall within the –4% region; these results were based on high-resolution seismic tomographic images at 40 km depth produced by *Zhao et al.* [2000].

To illustrate the correlation between volcano clusters and topography, a map was constructed using a hole-filled 90 m digital elevation model (DEM) derived from the Shuttle Radar Topography Mission data [*Jarvis et al.*, 2008]. This DEM was filtered in the Fourier domain using a 20 km low-pass filter to highlight comparatively long-wavelength topographic variation in the TVA (Figure 2a). Figure 2a shows that the volcano clusters correlate reasonably well with long-wavelength topographic highs. As discussed by *Tamura et al.* [2002] and by *Kondo* [2009], these topographic highs are only partially constructed from extrusive volcanic products. Much of the uplifted terrain is composed of metamorphic rocks—Miocene sandstone and mudstone. Given the ages of the uplifted terrain, the long-wavelength topography in the TVA is associated with uplift at rates that exceed typical tectonic values. For instance, local uplift rates in the Sengan cluster exceed 1 mm yr^{–1} [*El-Fiky and Kato*, 2006], whereas typical uplift rates are usually much less than 1 mm yr^{–1}.

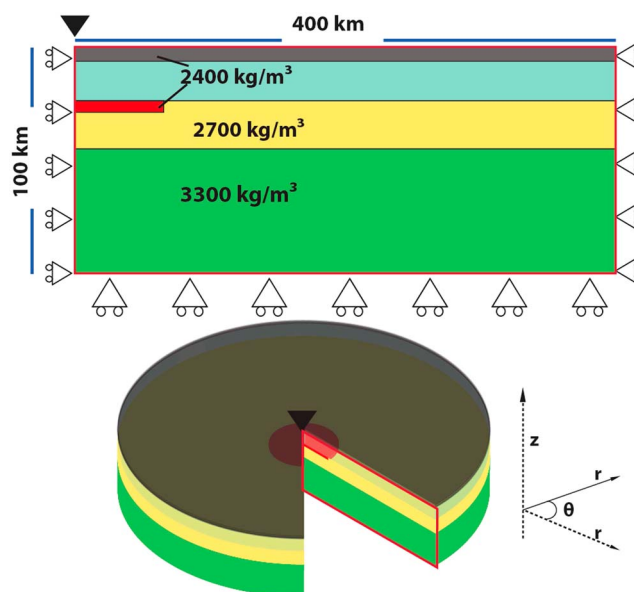


Figure 3. Schematic of the basic finite element model. (bottom) A 3-D solid of revolution is simulated by rotating (top) the 2-D plane around the axis of symmetry indicated by the black arrow. The model domain is divided into four main layers with the upper crust further subdivided into an elastic and viscoelastic layer. The corresponding density of each layer is also indicated on the plot and ranges from 2400 to 3300 kg/m³. The intrusion is represented by the red body; since this body is emplaced at the base of the lower crust in this schematic, its density is 2400 kg/m³. Boundary conditions are represented by the rollers which indicate the direction in which the model is allowed to move. On the left side of the domain, restricting the motion to only the vertical direction simulates symmetric conditions. Isostasy is simulated through the use of Winkler restoring forces applied at each horizontal density contrast boundary.

Bouguer gravity data for the TVA [Komazawa *et al.*, 2004] were filtered using a low-pass Gaussian filter with a half weight at 10 km to emphasize long-wavelength features (Figure 2c). A best fit linear trend was then removed from the filtered data to minimize the signal due to the subducting slab. Anomalous gravity lows occur along the arc, most distinct in the Sengan Cluster. In summary, volcano clusters correlate with tomographic anomalies in the asthenospheric wedge, relatively long-wavelength topographic highs, uplift, and gravity lows. These features are consistent with the hot zone and hot finger models of the arc and are best developed for the Sengan volcano cluster in Tohoku where volcanic vents are tightly clustered and mapped directly above a distinct gravity low. In the following we develop numerical models to link these observations and consider the ramifications specifically for the Sengan volcano cluster.

Significant questions remain regarding this conceptual model for the clustered nature of volcanism and associated geophysical observations. First, if significant hot zones are developed in the crust beneath volcano clusters, what is the depth of these hot zones? Are they formed at the Moho [Tamura *et al.*, 2002] or at shallower levels? What is the volume of magma in hot zones associated with the Quaternary volcano clusters of the TVA? How do these hot zones influence the geodynamics of the TVA, specifically the uplift rates within the arc? These questions are important to build upon our understanding of interplay between mantle dynamics, crustal magma intrusion, and the surficial expression of these processes—namely, arc volcanism and surficial uplift.

2.1.2. Axisymmetric Inversion of Regional Gravity Data

Addressing the questions posed in the preceding section requires the development of numerical models that represent a simplified version of this complex system without compromising the results. As a starting point for developing the numerical models that we will use to investigate these questions, an E-W gravity profile line is extracted along the Sengan Cluster at the location shown in Figure 2c. The data along this line are then inverted using an axisymmetric gravity model of a finite disk. To facilitate the comparison of the gravity anomaly generated by the finite disk with the observed gravity anomaly profiled across the Sengan volcano cluster, the gravity computations of triangular axisymmetric elements (more details will be provided in a later section) can be used to calculate the gravity signal at the surface. The raw gravity anomaly for the E-W profile at a given x location (distance from the axis of symmetry, and at an elevation of 200 m above the surface

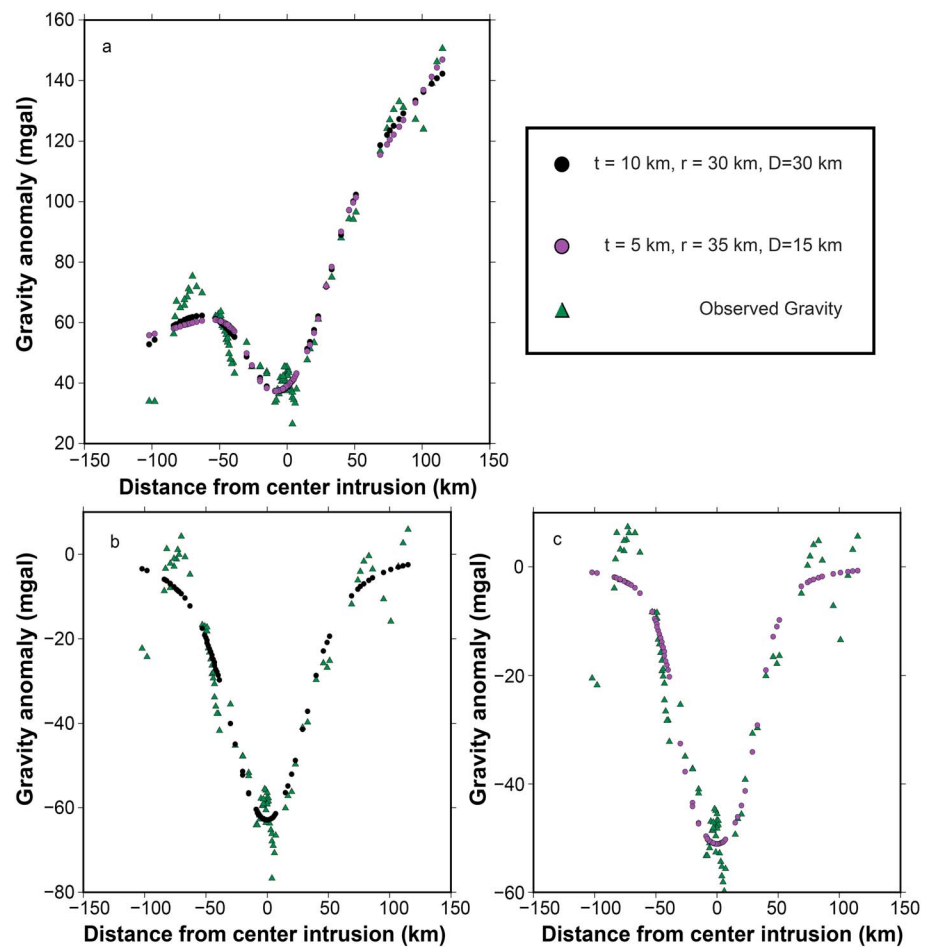


Figure 4. Fitting of a regional E-W profile, the location of which is shown in Figure 2, to a radial disk—in all subplots, the observed gravity data are represented by green triangles. (a) Axisymmetric gravity inversion of the E-W profile using 30–35 km radial disk at depths of 15 and 30 km (purple and black circles, respectively). These bodies have a thickness of 4–10 km and a density contrast of -430 to -658 kg/m^3 . (b and c) The fit of the axisymmetric gravity model to the data when a polynomial corresponding to the signal due to the subducting slab is removed from the data; the black circles represent a disk at a depth of 30 km, while the purple circles represent a body at 15 km. t = intrusion thickness, r = intrusion radius, and D = emplacement depth of the intrusion.

of the model, was computed using an order 8 Gaussian quadrature to integrate each triangular element of the 2-D cross section shown in Figure 3. Through this integration method, the corresponding gravity signal for the resulting axisymmetric element can be estimated using the element's density, depth, and dimensions. The surficial anomaly due to the intrusion and the dynamic topography at a particular x location is the sum of the individual elemental contributions within the entire domain. The linear inversion of the gravity data using this integration method returns the best fit density contrast for a disk at a given depth. The inversion results show that disks ranging in radius of 30–35 km and at depths of 15–30 km provide a good fit to the observed data (Figures 4a–4c), depending on the disk's density contrast. Inversion of the gravity data shows that disks emplaced at 15 km have a density contrast of -430 kg/m^3 , while those at 30 km have a contrast of -658 kg/m^3 . These large density contrasts required to model the gravity anomaly indicate that they may be associated with compositional differences (e.g., presence of differentiated magmas or hot, molten, and water-rich melts) in the hot zone. These inversion results helped define the intrusion geometry and density contrasts used in the numerical models described next.

2.2. Mechanical Model

Utilizing the finite element method code GTECTON, a number of axisymmetric, Maxwell viscoelastic models (linear relationship between stress and strain rate) are constructed and solved to evaluate the surface deformation induced by the buoyant forces associated with magma at different levels in the crust and with

different intrusion geometries. These models test the effect of varied depths, intrusion sizes, elastic layer thicknesses, and model rheologies by reducing the problem to the mechanical equilibrium between the deformation energy of the system and the internal forcing related to magma buoyancy. Axisymmetric models are utilized in problems where a 3-D solid of revolution can be generated by rotating a planar cross section 360°. Given that end-member models of magmatic bodies are frequently represented as cylinders or spheres [e.g., Gudmundsson, 2006; Aso and Tsai, 2014], the axisymmetric approximation used here is appropriate for describing the problem due to the symmetry of these shapes. In addition, the reduction of the 3-D problem to the equivalent 2-D problem greatly simplifies the computations, which in turn speeds up the analysis and allows for a thorough and efficient examination of the necessary parameter space. In the case of solids of revolution about the z axis, r refers to the radial direction and θ to the tangential direction (see Figure 3). Displacements and displacement gradients are assumed to be 0 in the θ direction, so that strain tensor components $\epsilon_{r\theta} = \epsilon_{\theta z} = 0$. The constitutive equations for a combination of a compressible elasticity and incompressible power law viscosity are

$$\left\{ \begin{array}{l} \dot{\epsilon}_{rr} = \frac{1}{E} (\dot{\sigma}_{rr} - \nu(\dot{\sigma}_{zz} + \dot{\sigma}_{\theta\theta})) + \frac{(\sigma_E/\eta_{\text{eff}})^{n-1}}{6\eta_{\text{eff}}} (2\sigma_{rr} - \sigma_{zz} - \sigma_{\theta\theta}) \\ \dot{\epsilon}_{zz} = \frac{1}{E} (\dot{\sigma}_{zz} - \nu(\dot{\sigma}_{rr} + \dot{\sigma}_{\theta\theta})) + \frac{(\sigma_E/\eta_{\text{eff}})^{n-1}}{6\eta_{\text{eff}}} (2\sigma_{zz} - \sigma_{rr} - \sigma_{\theta\theta}) \\ \dot{\epsilon}_{\theta\theta} = \frac{1}{E} (\dot{\sigma}_{\theta\theta} - \nu(\dot{\sigma}_{rr} + \dot{\sigma}_{zz})) + \frac{(\sigma_E/\eta_{\text{eff}})^{n-1}}{6\eta_{\text{eff}}} (2\sigma_{\theta\theta} - \sigma_{rr} - \sigma_{zz}) \\ \dot{\epsilon}_{rz} = \frac{1+\nu}{E} \dot{\sigma}_{rz} + \frac{(\sigma_E/\eta_{\text{eff}})^{n-1}}{2\eta_{\text{eff}}} \sigma_{rz} \end{array} \right\},$$

where $\dot{\epsilon}_{ij}$ are components of the strain rate tensor, a dot indicates differentiation with respect to time, E is Young's modulus, ν is Poisson's ratio, σ_{ij} are components of the Cauchy stress tensor, η_{eff} is the effective viscosity, and the effective shear stress σ_E derives from the second invariant of the deviatoric stress tensor:

$$\sigma_E = \sqrt{\frac{\sigma_{rr}^2 + \sigma_{zz}^2 + \sigma_{\theta\theta}^2 - \sigma_{rr}\sigma_{zz} - \sigma_{rr}\sigma_{\theta\theta} - \sigma_{zz}\sigma_{\theta\theta}}{3} + \sigma_{rz}^2}.$$

Matrix equations are solved using Portable, Extensible Toolkit for Scientific Computation (PETSc) implemented in *OpenMPI*, a suite of data structures and routines for the scalable solution of partial differential equations [Balay et al., 2002]. The new axisymmetric code was benchmarked extensively, including comparisons to analytical results. Tests used for benchmarking the code include models of a finite pressurized sphere buried in an elastic half space [McTigue, 1987], a thick cylindrical elastic tube under internal pressure [Timoshenko and Goodier, 1951], and a circular Kirchhoff plate bent under an axial load [Brotchie and Silvester, 1969].

2.2.1. Model Geometry

The basic finite element model in this study is defined by a domain that is 400 km in radius and subdivided vertically into four major layers representing an average Tohoku lithosphere [Furukawa and Uyeda, 1989; Hasegawa et al., 1993; Zhao et al., 1990]. The model dimensions and boundary conditions as well as the layer properties are fully described in Figure 3 and Table 1. Although the refinement of the overall domain may vary among the different modeled scenarios detailed below, the basic mesh refinement involves subdividing the main layered domain using the *triangle* code developed by Shewchuk [1996, 2002] to implement the Delaunay triangulation scheme [Chew, 1993; Ruppert, 1995]. Convergence testing of various model domains showed that a radius of 400 km and a vertical extent of 100 km creates a large enough domain dimension to prevent edge effects that would distort the signal of interest. Additionally, the convergence testing showed that the simulations were insensitive to further grid refinement. Within the larger domain, radial intrusions ranging from 30 to 60 km diameter and thicknesses of 0.5–4 km are emplaced at either the Conrad discontinuity (15 km depth) or the Moho (30 km). These model radii capture the extreme ranges of underplating bodies in Tohoku [Tamura et al., 2002] and the results of the preliminary axisymmetric gravity inversion and hence are useful for making inferences about the deformation due to other intrusion sizes. It should be noted that the thicknesses of the disks cannot be well constrained using only gravity data since there is a trade-off between modeling the density contrast and the disk thicknesses. However, field observations of unroofed plutons show a range of intrusion sizes that are consistent with the models used here [e.g., Grocott et al., 2009 and Leuthold et al., 2014].

Studies have shown that large composite volcanoes in the arc may remain active for periods as long as 10^5 to 10^6 years [Hildreth, 1981; Thouret, 1999; Davidson and De Silva, 2000]. Assuming that the magma source,

Table 1. General Summary of Key Model Parameters^a

Layer	Thickness (km)	Density Contrast (kg/m ³)	Viscosity (Pa s)
Elastic upper crust	0–7	-	10 ³⁰
Upper crust	15	-	10 ²¹
Conrad intrusion	1	-300	10 ³⁰
Lower crust	15	-	10 ¹⁹
Mantle	70	-	10 ²² (10 ¹⁹)

^aLayer viscosity for the crème brûlée rheological models are given in parentheses in the fourth column where they differ from the jelly sandwich value. Viscosities of 10³⁰ Pa s ensure that the layer behaves elastically on the timescale of the simulation. The density contrasts given here are between the intrusion and the layer in which it is embedded.

i.e., the hot zone, must remain stable at least an equivalent time period, all numerical models in this study are integrated for 1 Myr. This time frame also coincides with the minimum stable period of SSCs modeled by *Davies et al.* [2016].

2.2.2. Boundary Conditions

The boundary conditions are kept uniform across all the models. At the axis of symmetry (left side in Figures 4–9), motion is only allowed in the vertical direction. Similar boundary conditions are maintained on the outer edge of the model (right side of the models in Figures 4–9). The top of the model is treated as a free surface and hence is allowed to deform freely; motion is only allowed in the horizontal direction along the base of the model (see Figure 3). Isostasy is simulated through the use of Winkler restoring forces at each of the layer interfaces [*Desai, 1979; Williams and Richardson, 1991; Wallace and Melosh, 1994; Desai and Kundu, 2001*].

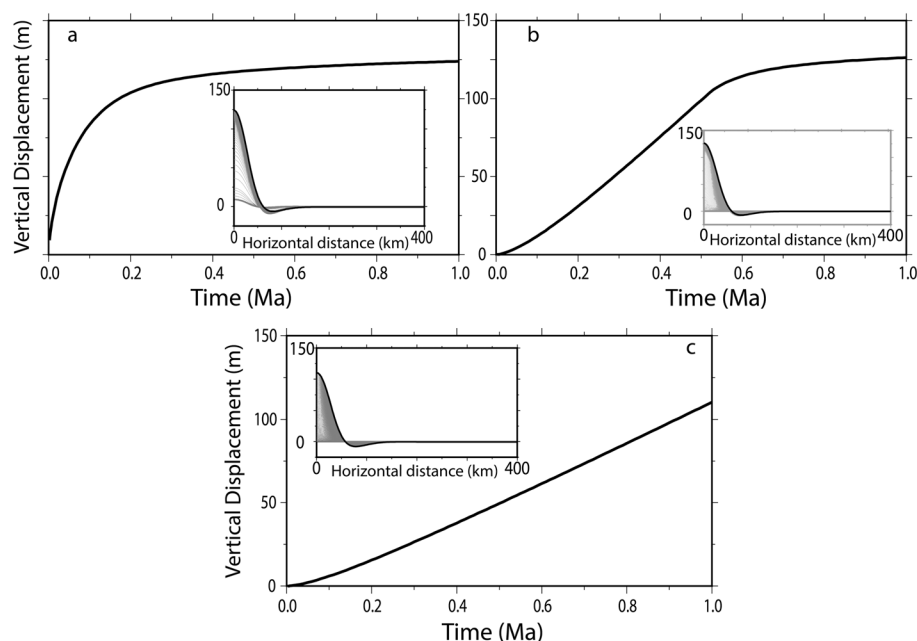


Figure 5. Summary plots of the surficial response due to an incremental intrusion. (a) History of the surface vertical displacement due to the instantaneous intrusion of a magmatic body with radius 30 km and a thickness of 1 km at the Conrad discontinuity (same as the solid black curve in Figure 6). In the main plot, the history of vertical displacement of a point above the center of the intrusion is shown, while the inset figure shows the deformation history from the beginning of intrusion to 1 Myr (heavy black curve); the deformation curves are plotted every 10 kyr. (b) The main plot shows the history of the surface vertical displacement when the body shown in Figure 5a is intruded gradually during a 500 kyr period; following the end of intrusion, deformation continues linearly for a short period then proceeds asymptotically to roughly the same value as in Figure 5a. The inset shows the deformation of the top surface at various time intervals. (c) In this plot, the magmatic body in Figure 5a is intruded continuously over the course of the model run (1 Myr). The vertical deformation increases linearly with time but does not reach the same peak amplitude as in Figure 5a or 5b.

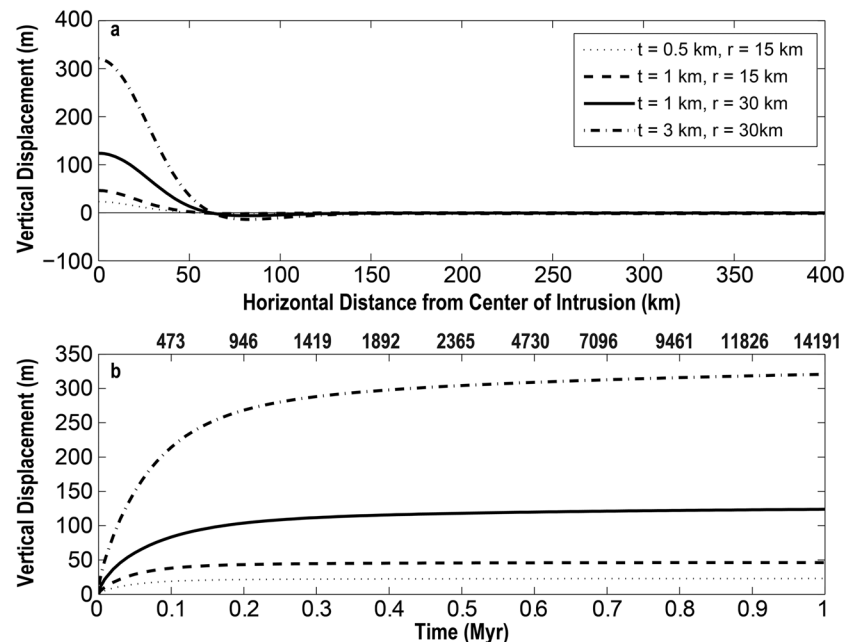


Figure 6. (a) Each curve represents the vertical deformation of the surface layer due to 30 km, and 15 km radial bodies emplaced at the Conrad discontinuity 1 Myr after start of the model run. The maximum displacement of about 325 m with a wavelength of about 50 km (solid black curve) is seen in the 30 km radius body (3 km thick), while the smallest displacement (~ 25 m) is seen in the intrusion having a radius of 15 km and a thickness of 0.5 km. (b) The deformation history of the point at the surface directly above the intrusion is shown. For all the geometries tested, the initial deformation of this point occurs rapidly within the first 100,000 years then proceeds at a more gradual pace for the remainder of the model run. The wavelength of the deformation remains relatively constant among the three geometries shown here, but the peripheral basin tends to be underdeveloped in the smaller geometries. Bold numbers on the top of Figure 6b are the minimum Maxwell time for the model. t = intrusion thickness and r = intrusion radius.

2.2.3. Material Properties

In these models, constant Maxwell rheology is utilized in each layer since we expect the buoyancy force associated with the ponded magma to produce an instantaneous elastic response followed by viscous relaxation. To derive the viscosity assigned to each layer, the values from the given strength envelopes and common literature values are averaged [Dixon *et al.*, 2004; Bürgmann and Dresen, 2008; Artemieva, 2011; Iwasaki *et al.*, 2013]. These viscosity values range from 10^{19} to 10^{21} Pa s. To simulate the elastic property of a layer (e.g., the elastic layer or intrusion shown in Figure 3), the viscosity is set to an arbitrarily high value (10^{30} Pa s) so the layer would not undergo viscous behavior within the time frame of the model simulation (1 Myr). Setting the viscosity of the intruded body is a more complex issue. Due to the number of factors that influence the characteristics of the hot zone such as the magma properties, percentage of melt, and characteristics of the country rock, the actual viscosity of the bulk of the hot zone is not very well constrained. In the initial tests that we performed using relatively low viscosities (10^{17} Pa s), we found that very small time steps were needed to maintain the model stability due to internal deformation of the intrusion; here internal deformation was in the form of slight up-warping near its center. We chose to use higher viscosities (10^{30} Pa s) in the full simulations since the change in the shape of the intrusion was small for these different viscosities but the computation time was drastically reduced. In general, on the timescales under investigation (hundreds of kyr), the difference in shape of the intrusion between the low viscosity and higher viscosity intrusion models is not large enough to significantly alter the overall results produced in this study.

In all the numerical models presented below, the driving force is the buoyancy force induced by the density contrast between the intrusion and the layer that it intrudes. For bodies underplated at the Conrad discontinuity, the density contrast is set to -300 kg/m³, while intrusions underplated at the Moho have a density contrast of -600 kg/m³. This change in density contrasts was defined to be consistent with the results of the gravity inversions discussed previously and with hot zone models in which mafic melt originally emplaced at great depths in the lithosphere gradually differentiates and segregates from the larger mush ponds [Solano *et al.*, 2012]. These differentiated melts ascend through the crust intermittently [Menand *et al.*, 2015]

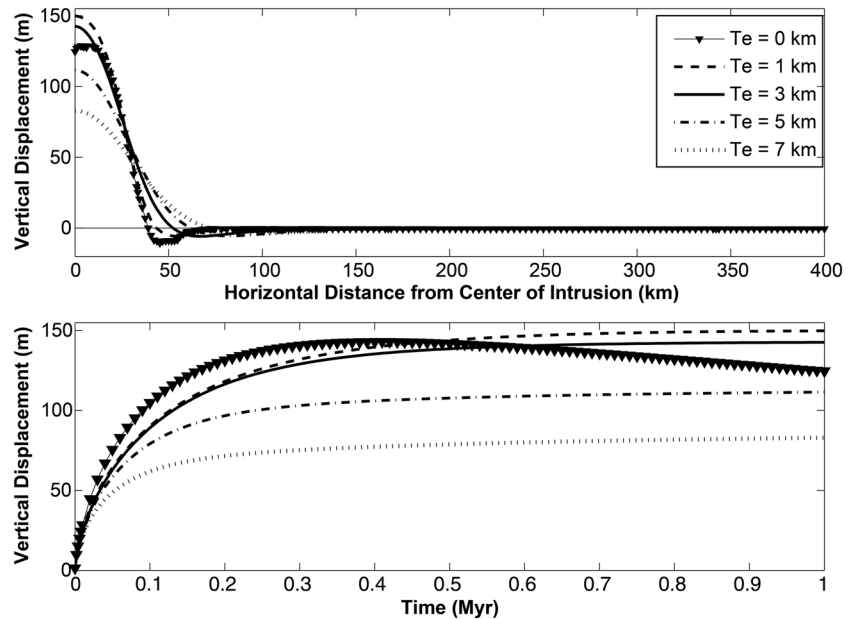


Figure 7. (a) Vertical displacement driven by a 30 km radius intrusion in a viscoelastic Maxwell model with elastic layer thicknesses of 0 km (triangles curve), 1 km (large dashed line), 3 km (solid curve), 5 km (dash-dotted curve), and 7 km (short dashed curve) after 1 Myr. The maximum displacement among these models is about 120 m seen in a model with elastic layer thickness of 3 km. This displacement has a peak amplitude that is ~25 m greater and a wavelength approximately 3 times larger than the corresponding values in the model with no elastic layer. (b) The deformation history is similar for each of these models except when the upper crust has no elastic layer; for this model, the peak topography begins to subside about 600 kyr after the intrusion is emplaced. Bold numbers on the top of Figure 7b are the minimum Maxwell time for the model.

where they may become stalled for a number of reasons, such as encountering a stress barrier unfavorable to vertical magma propagation [Gudmundsson, 2011] or reaching a point of neutral buoyancy. These stalled melts will form the underplated bodies that drive the surficial deformation. Repetition of this differentiation, segregation, and emplacement process may eventually result in the emplacement of silicic magma bodies at relatively shallow levels.

2.2.4. Initial Conditions

Stresses are taken to be isotropic initially, so that all deformation results from magma emplacement since (model) time = 0. Also, the model is initially taken to be in isostatic equilibrium so that vertical surface displacements are due to the magma emplacement only. The mechanics of sill emplacement is very complex and not completely understood; however, we expect this process to produce a quasi-instantaneous elastic

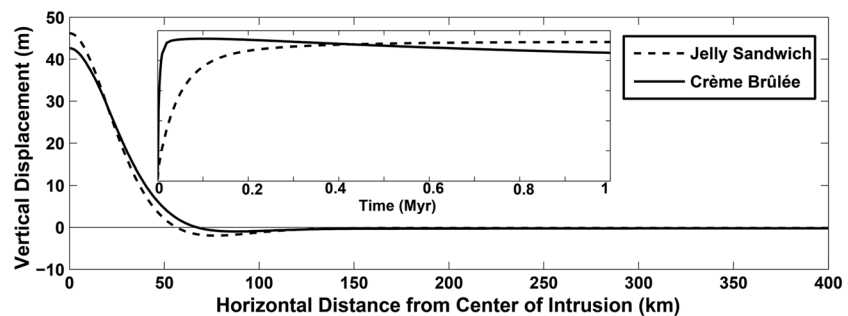


Figure 8. Vertical displacement due to a 15 km radius body emplaced at 15 km depth in a crème brûlée rheological model (solid curve) and a body of the same size emplaced in a jelly sandwich model (dashed curve). The vertical deformation in these two models show similar peak amplitude, but the history of said deformation varies significantly. The maximum deformation occurs well within the first 50 kyr after intrusion emplacement and then proceeds asymptotically for nearly the full model run before beginning to subside in the crème brûlée rheological model; in the jelly sandwich model, the uplift occurs at a slower pace and there is no subsidence.

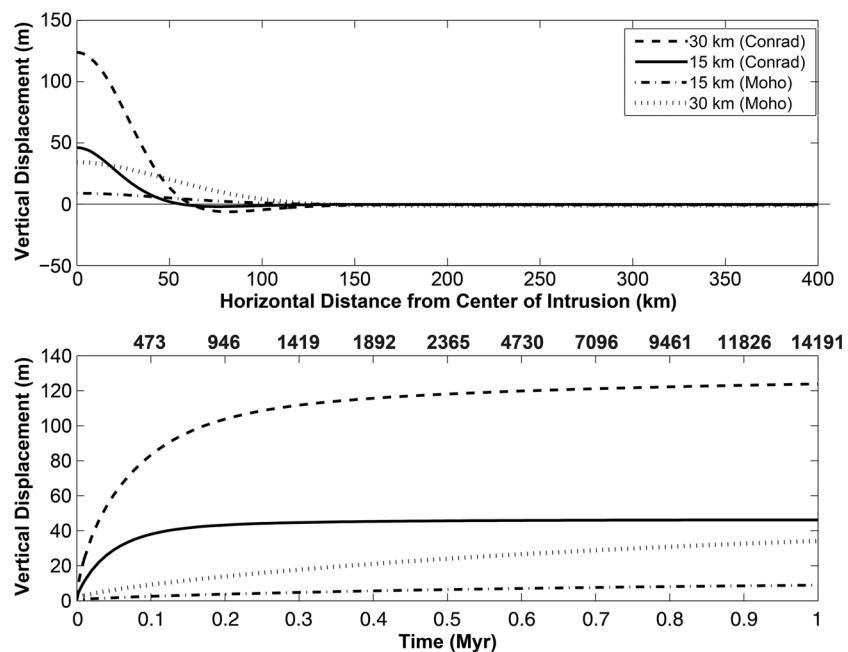


Figure 9. Vertical displacement plots for (top) intrusions 30 and 15 km in radius emplaced at the Conrad (15 km depth) or the Moho (30 km) 1 Myr after emplacement and (bottom) deformation history for the point above the center of the intrusion. Here the 15 and 30 km radial intrusions emplaced at the Conrad are represented by the solid and large dashed curves, respectively; these models produce a larger-amplitude, shorter-wavelength deformation almost instantaneously that quickly levels off. On the other hand, models in which the intrusions are emplaced at the Moho produce a smaller-amplitude, longer-wavelength displacement. Deformation proceeds slowly with both sizes of intrusion tested and does not appear to have reached its peak value even after 1 Myr. Bold numbers on the top of Figure 9 (bottom) are the minimum Maxwell times for the model; in most model scenarios, deformation increases exponentially for several thousand relaxation cycles before reaching an asymptotic level.

deformation on timescales much shorter than the long-term dynamic topographic response to a low-density hot zone which is the end goal of this study. As such, we do not explicitly model the deformation due to the sill opening in this study but rather focus on the dynamic support and uplift rate associated with the buoyant intrusions, which will operate on a longer timescale.

3. Results

The complexity of lithospheric response necessitates the evaluation of a number of parameters to properly understand the impacts of hot zone development on the long-term surficial response. We begin by illustrating the surficial response to the incremental intrusion of magma at various rates. We then investigate the consequences of varying the depth and size of the hot zone, as well as the rheological properties of the model domain when the buoyant forces are due to an accumulated volume of magma. The results of the simulations are shown as the time history of deformation at the center of the intrusion and the vertical displacement of the surface as a function of distance after 1 Myr.

3.1. Incremental Intrusion

The development of crustal and subcrustal magma bodies may occur through an incremental process in which large magma chambers are built up by several sills [Solano *et al.*, 2012; Menand *et al.*, 2015]. For a viscoelastic numerical model, like the ones used here, the history of magma emplacement may play a significant role in the overall deformation pattern. On short timescales, a viscoelastic material behaves like an elastic body, but if intrusion occurs over a time period comparable to the relaxation time, the body will begin to relax the stresses induced by buoyancy forces and induce creep in the surrounding rocks. The final topography will reflect the interplay between the buoyancy forces, the dynamic topography induced by the flow (decreasing with time), the viscous resistance, and the effective elastic strength of the lithosphere which attempts to hold the body in place. It therefore follows that if the intrusion is instantaneous, the lithosphere will be affected by an instantaneous elastic response followed by an exponential decay of the stresses in the region surrounding

the intrusion. On the other hand, an incrementally emplaced intrusion will cause the crust to be constantly loaded while it relaxes the stresses accumulated by the previous history of emplacement. The final deformation varies as a function of the rate of intrusion, the duration of the magma emplacement history, and their relationship with the relaxation time. Given the linear nature of the system analyzed in this study, the influence of the continuous load and relaxation can be modeled through a convolution of the history of magma emplacement and the history of the deformation due to the intrusion of a unit body [Fung and Tong, 2001].

Figure 5 shows the history of the vertical displacement of the point at the center of the magma emplacement for three different intrusion rates: an instantaneous intrusion, an intrusion in which the body increases linearly for the first 500 kyr, and one where intrusion occurs for the entire model run (1 Myr). Given that the bulk relaxation of the system is shorter than 0.5 Myr in these models (as indicated by the time necessary to reach steady state in the rheological model comparisons (subsection 3.4 discussed below), the total vertical displacement of the first two cases is not significantly different after 1 Myr. The significant variations in these models are seen in the history of deformation. For the first case (Figure 5a), the vertical displacement quickly increases in the years after the magma emplacement and the vertical rate decreases exponentially. In the second case, the topography increases in a much smoother way (almost linearly) until the end of the intrusion time. This suggests that there is a substantial equilibrium between loading and relaxation. The system then recovers the remaining deformation with an exponential decrease of the vertical velocity after the intrusion stops. In the last scenario, the system does not have time to relax indicating a larger apparent elastic strength. The result is a final topography that is smaller than in the previous two scenarios.

3.2. Effect of Intrusion Size

The deformation of the top surface of the model resulting from tests in which the intrusion sizes are varied is illustrated in Figure 6. The peak vertical displacement occurs on the axis of symmetry, just above the center of the intrusion. The elevated topography is bounded by a shallow peripheral trough defined by elevations below the original undeformed topographic surface (e.g., black horizontal line in Figure 6). The peripheral basin is located approximately 50 to 70 km away from the center of the model. This deformation pattern closely mirrors the topographic highs and surrounding trough seen in volcanic areas such as Tohoku or Uturuncu Volcano, Bolivia [Sparks *et al.*, 2008]. In Figure 6, the surface topography at the center of the intrusion increases rapidly after the instantaneous intrusion, tending asymptotically to a value significantly lower than that expected by isostatic equilibrium, which was calculated to be ~ 270 m [Watts, 2001] for the density distribution used in these models (see Table 1).

3.3. Effect of Elastic Layer Thickness

The elastic thickness of the lithosphere has been defined in a number of different ways by various researchers. Primarily, estimates of the elastic thickness are based on the thickness of the seismogenic zones as a proxy [e.g., Maggi *et al.*, 2000], gravity and topography/bathymetry admittances [Kruse *et al.*, 1997; Watts, 2001; Audet and Bürgmann, 2011], studies of material properties such as Young's modulus and Poisson's ratio [Burov and Diament, 1995], or elastic thickness/stresses modeling [Tesauro *et al.*, 2013]. Additionally, potential field data can be used to estimate the thickness of the elastic layer [Flück *et al.*, 2003; Burov and Watts, 2006; Tiwari *et al.*, 2006; Jellinek *et al.*, 2008; Pilkington and Saltus, 2009]. For the most part, these different methods give fairly consistent values for the elastic layer thickness estimates; the values range from 5 to 190 km with thickness of 5–20 km being common in young orogens and thickness > 60 km most common in old cratons. For instance, Kruse *et al.* [1997] found elastic thicknesses of 1–4 km for the youngest seamounts of the Easter Seamount Chain and a maximum of 11 km in the older seafloor on the eastern end of the chain. In this study, elastic layer thicknesses of 0, 1, 3, 5, and 7 km were tested to explore the effects that this parameter has on the deformation. While these values run on the low side, they are appropriate for active volcanic regions where the increased heat flux is expected to reduce the strength of the crust. Based on the thickness of the seismogenic zone beneath the TVA, an elastic layer thickness of 7 km would be most valid [Hasegawa *et al.*, 1993].

The resulting deformation after 1 Myr due to a 30 km radius intrusion (Figure 7) shows that the thickness of the elastic crust may exert a stronger control over the wavelength and amplitude of the displacement than does the radius of the intrusion. In models where no elastic thickness was assigned (the triangle marked curve in Figure 7), the wavelength of the anomaly is relatively short, mimicking the dimension and shape of the magmatic intrusion. The wavelength of the displacement increases as the thickness of the elastic layer increases. The slope of the topography decreases significantly, and the depocenter of the peripheral basin moves farther away from the center of the intrusion and shallows significantly. A corresponding decrease in the maximum

amplitude of the vertical displacement accompanies this increase in wavelength. The maximum amplitude in the model with no elastic thickness is ~ 140 m, while a 7 km elastic layer model has a peak amplitude of ~ 85 m.

As a consequence of the viscoelastic behavior of the chosen rheology, even in the absence of a purely elastic layer, the system does not reach full isostatic equilibrium (~ 270 m of uplift). While all the models with an elastic layer reach and maintain a peak topographic high after a few Maxwell relaxation intervals, the model with no elastic layer tends to slowly subside once its maximum level has been reached due to lateral viscous flow of the upper crust (Figure 7b triangles).

3.4. Rheology: Crème Brûlée Versus Jelly Sandwich Rheology

Two opposing models of crustal rheology have been proposed by *Chen and Molnar* [1983] and *Jackson* [2002]. The main feature of the jelly sandwich model [*Chen and Molnar*, 1983] is a weak lower crust sandwiched between a mechanically strong upper crust and upper mantle. This model is appropriate in settings where the crust is overthickened such as in the Andes or Tibet [*Meissner and Mooney*, 1998; *Beck and Zandt*, 2002; *Zandt et al.*, 2004]; overthickening may result in partial melting of the lower crust as radioactive elements become concentrated and eventually decay giving off thermal energy. In *Jackson's* crème brûlée model, the strong upper crust sits atop a mechanically weak lower crust and upper mantle. The weakness of these layers is thought to be a consequence of the high mantle temperatures and the addition of water into the system.

To model the crème brûlée rheology, the mantle viscosity is dropped to 10^{19} Pa s while all other layer viscosities are kept the same as in the jelly sandwich model (see Table 1). Figure 8 allows for a direct comparison of the deformation associated with a 15 km radial intrusion emplaced at 15 km depth in a crème brûlée (solid curve) rheological model to the deformation generated by an intrusion of the same dimensions (dashed curve) in the jelly sandwich model. A comparison of these two model outputs shows that while the overall value of the displacement does not vary dramatically, the time history of the deformation is vastly different. In Figure 8 (inset), the maximum displacement is reached within less than 100,000 years of emplacement for the crème brûlée model; this level is not reached in the jelly sandwich model until the end of the model run (1 Ma). Additionally, the surface begins subsiding soon after the peak deformation is reached in the weak mantle model, while uplift continues in the jelly sandwich model to the end of the run. The rapid deformation in the crème brûlée model is likely due to the low mantle viscosity, which allows material to flow easier under the influence of the applied buoyancy forces (see supporting information Figure S1). The model quickly reaches its new equilibrium state following the intrusion, and any further deformation proceeds slowly. The higher mantle viscosity in the jelly sandwich model significantly hinders the flow of material from the upper mantle which results in slower model equilibration.

3.5. Varying the Depth of the Intrusion

Studies by *Hasegawa et al.* [1993] have found large regions of low velocity at various depths in the crust. These zones tend to occur prominently beneath the active volcanic vents, reaching depths as shallow as 7 km beneath the surface in some localities. In this set of experiments, the magmatic intrusions were emplaced at depths of 15 and 30 km beneath the surface to investigate the impact that emplacement depth has on the surface displacement. Figure 9 shows our estimates of surface displacement 1 Myr after intrusion for bodies emplaced at the Conrad or the Moho. The maximum vertical displacement for the bodies underplated at the Moho is approximately 35 and 10 m for the 30 and 15 km radius intrusions, respectively. These values are smaller than the peak amplitudes of 125 and 45 m reached in the models with intrusions of the same size emplaced at the Conrad discontinuity. Accompanying this decrease in amplitude is an increase in the wavelength of the vertical displacement; in the Moho underplating models, the wavelength is about 100 km which is about 2 times that generated by the shallower intrusion.

These deep emplacement models also differ significantly in the deformation history from the shallow emplacement models. In the Conrad discontinuity intrusion models, the initial deformation attained its asymptotic value relatively quickly, reaching a peak value within the first few hundred thousand years. In the Moho underplating models, the vertical deformation increases much slower with a very small decrease in the vertical velocity. From Figure 9, it appears that the vertical displacement never reaches its asymptotic value even after 1 Myr; this is an indicator that the bulk relaxation time of the system is much longer for this model setup. This is comparable to the deformation results obtained when the intrusive bodies are emplaced at the Conrad discontinuity in a “jelly sandwich” model (Figure 8); in these models, deformation was primarily accommodated by flow within the low viscosity lower crust (short relaxation time). Underplating at the Moho forces a deflection of the discontinuity that must be accommodated by flow within the mantle which has a

higher viscosity and hence a longer relaxation time. The cross sections in supporting information Figure S1 show the flow vectors for the crème brûlée and jelly sandwich models for intrusions emplaced at depths of 15 and 30 km.

4. Discussion

Numerical modeling indicates that the gravity anomalies and deformation patterns observed in the TVA are associated with processes operating in the crust, possibly to depths as great as the Moho, rather than in the asthenosphere. Although the magma source region may be dictated by the occurrence of hot fingers in the asthenosphere, the magnitude and wavelength of the uplift and gravity anomalies are inconsistent with mantle depths. Instead, the results of axisymmetric gravity inversion indicate that density anomalies occur in the crust or at the Moho (yielding a large required density contrast). These depths are consistent with geodynamic model results, which show that dynamic topography can be supported by intrusions in the crust. These results are consistent with the development of a hot zone beneath the Sengan cluster. Conversely, these features cannot directly result from the presence of hot fingers.

The underplating of buoyant material at a layer boundary will exert an upward force on the overlying layers which will result in surface deformation. There are a number of physical conditions that dictate the manner in which deformation proceeds. For instance, our investigation of the effect of intrusion size shows that the exponential increase in elevation with time since intrusion is mainly controlled by the viscoelastic response of the lithosphere, while the departure of the model topography from isostatic equilibrium is likely a consequence of the strength of the lithosphere (particularly the elastic portion) restricting the deformation of the magmatic body. In a purely viscous regime, the magmatic body is expected to rise to its isostatic position. In addition to controlling the total uplift, the strength of the lithosphere is also responsible for the shape of the peripheral basin surrounding the topographic high. While the peak deformation amplitude appears to scale linearly with the dimensions of the intrusion, the wavelength of deformation remains relatively constant. Further parameter testing showed that the wavelength of deformation was strongly influenced by the thickness of the elastic layer, while the flexural rigidity of the model may play a role in limiting the maximum height of the dynamic topography.

Another important factor influencing the time needed to reach the steady state topography is the bulk relaxation time of the system. This was illustrated in several sections; in the first instance, by lowering the viscosity of the mantle in the crème brûlée model, the viscosity and hence the relaxation time of the system is reduced. When a magmatic body is placed in the jelly sandwich rheological regime at the Conrad discontinuity, the deformation is mainly accommodated through flow within the lower crust. The flow within the mantle is negligible; hence, the deformation at the Moho is not significant. On the other hand, the deformation in the presence of a weak mantle is accommodated by flow both in the lower crust and the mantle accompanied by possibly deflection of the Moho discontinuity. Enhanced mantle flow in the crème brûlée model occurs within 100 km of the intrusion center. In the second instance, emplacement of a magmatic body at the Moho in the jelly sandwich model leads to the conclusion that the observed bulk relaxation time of the “jelly sandwich” system is mainly controlled by the lower crust viscosity when underplating occurs at the Conrad discontinuity and by the mantle when the underplating is happening at the Moho. This results in a longer relaxation time of the system when the mantle viscosity is high. Finally, in the incremental intrusion section, we have shown that the deformation pattern of the system changes in response to the time history of intrusion. When the intrusion is modeled as instantaneous, the system has time to recover to its equilibrium state. In contrast, continuous intrusion prevents the system from relaxing, and deformation increases for the entire time span of the simulation.

5. Conclusions

Given the strong correlation between topography, volcano clusters, and geophysical anomalies (gravity anomalies or seismic velocities) in the TVA, a full understanding of the long-term evolution of this volcanic system requires an integrated evaluation of these phenomena. The models presented above do just that; the results of our models indicate that development of hot zones in the crust, perhaps as deep as the Moho discontinuity, could generate dynamic support that potentially affects local uplift and denudation rates. The deformation wavelengths show that enough support could be generated by these bodies to uplift regions within a radius of 50 km or greater from the center of the intrusion. The observed surface deformation

represents a balance between the lithospheric rheology, the intrusion geometry, and the thickness of the elastic layer. Our results also confirm the observations of *Tamura et al.* [2001] suggesting that current seismic velocity and gravity anomalies localized in the “hot fingers” play an important role in understanding the future evolution of the regional uplift and denudation rates. Rates of modeled and observed surficial uplifts are in good agreement. For example, *Litchfield et al.* [2009] show 40–100 m of uplift beneath the volcanic centers during the last 100 kyr. This uplift rate falls in the range of uplift rates produced by our models of intrusions emplaced at 15 km depth (Conrad); these intrusions were modeled as 1 km thick circular disc of radius 15 to 30 km. Modeled intrusions with thicknesses greater than 1 km produced uplifts that are close to those measured by *Tamura et al.* [2002] (about 500 m) and may reflect crustal response to a longer timescale of magmatic intrusions (see Figure 6). Our modeling results therefore show that the surficial uplifts within the TVA are best modeled by midcrustal intrusions rather than bodies situated at the Moho.

The close match of the modeled uplift rates with the observations are further supported by gravity data inversions. Using an axisymmetric model of a finite disk to invert the data shows that at least for the Sengan volcano cluster, local gravity lows are best modeled by ~30 km radius bodies underplated at depths of 15 to 30 km with density contrasts of -430 to -658 kg/m³. The tight clustering of volcanic vents within the Sengan volcano cluster as opposed to the more dispersed distribution of vents elsewhere in the TVA suggests that this cluster is well developed. Therefore, when coupled with the high-silica eruptive products at the center of the cluster [*Ueki and Iwamori*, 2007] and the results of our gravity model, the Sengan cluster is consistent with a hot zone [*Tamura et al.*, 2002; *Annen et al.*, 2006].

Our results suggest that the topography and gravity anomaly observed above the “hot finger” in the Sengan volcano cluster are mainly related to magma intrusion at middle to lower crustal levels, instead of within the asthenospheric wedge as suggested by *Tamura et al.* [2001]. If magmatism, underplating, and dynamic topography are strongly coupled with the long-lived mantle instability that gives rise to the asthenospheric hot fingers, the current observations should be stable for time frames of 1 Myr or more. In general, in the absence of particularly “fast” phenomena, such as slab retreat or slab tear, the timescale to change the dynamics of the mantle is on the order of several million years [*Honda and Saito*, 2003; *Honda et al.*, 2010; *Davies et al.*, 2016]. Therefore, based on their numerical simulations [*Honda and Saito*, 2003; *Honda et al.*, 2010; *Davies et al.*, 2016], we expect the “hot finger” suggested by *Tamura et al.* [2001] to be a stable feature at least on the timescale of 1 Myr.

Acknowledgments

This work was made possible through funding from the NUMO (Japan) evaluating tectonic aspects of the siting of geological repositories for radioactive wastes (Topaz project). Additional funding was provided by the NSF FGLSAMP Bridge to the Doctorate award HRD 1139850. This manuscript was greatly improved by helpful comments from R.S.J. Sparks, Catherine Annen, and an anonymous reviewer. The authors are grateful for discussions about the geodynamics of volcano clustering in the TVA with Jun Goto, Neil Chapman, and other members of the TOPAZ team. All numerical simulations were conducted using the new axisymmetric code implemented in GTECTON; the code and input files are available from the corresponding author upon requests. All other data for this paper are properly cited and referred to in the reference list.

References

- Annen, C., J. Blundy, and R. Sparks (2006), The genesis of intermediate and silicic magmas in deep crustal hot zones, *J. Petrol.*, *47*(3), 505–539.
- Annen, C., J. D. Blundy, J. Leuthold, and R. S. J. Sparks (2015), Construction and evolution of igneous bodies: Towards an integrated perspective of crustal magmatism, *Lithos*, *230*, 206–221.
- Artemieva, I. M. (2011), Flexure and rheology, in *The Lithosphere—An Interdisciplinary Approach*, vol. 1, chap. 8, pp. 505–541, Cambridge Univ. Press, New York.
- Aso, N., and V. C. Tsai (2014), Cooling magma model for deep volcanic long-period earthquakes, *J. Geophys. Res. Solid Earth*, *119*, 8442–8456, doi:10.1002/2014JB011180.
- Audet, P., and R. Bürgmann (2011), Dominant role of tectonic inheritance in supercontinent cycles, *Nat. Geosci.*, *4*(3), 184–187, doi:10.1038/ngeo1080.
- Balay, S., W. D. Gropp, L. C. McInnes, and B. F. Smith (2002), Software for the scalable solution of partial differential equations, in *Sourcebook of Parallel Computing*, edited by J. Dongarra et al., pp. 621–647, Morgan Kaufmann, San Francisco, Calif.
- Beck, S., and G. Zandt (2002), The nature of orogenic crust in the central Andes, *J. Geophys. Res.*, *107*(B10), 2230, doi:10.1029/2000JB000124.
- Bott, M. (1953), Negative gravity anomalies over acid “intrusions” and their relation to the structure of the Earth’s crust, *Geol. Mag.*, *90*(4), 257–267.
- Brotchie, J., and R. Silvester (1969), On crustal flexure, *J. Geophys. Res.*, *74*(22), 5240–5252.
- Bürgmann, R., and G. Dresen (2008), Rheology of the lower crust and upper mantle: Evidence from rock mechanics, geodesy, and field observations, *Annu. Rev. Earth Planet. Sci.*, *36*(1), 531–567, doi:10.1146/annurev.earth.36.031207.124326.
- Burov, E. B., and M. Diament (1995), The effective elastic thickness (T_e) of continental lithosphere: What does it really mean?, *J. Geophys. Res.*, *100*(B3), 3905–3927, doi:10.1029/94JB02770.
- Burov, E. B., and A. B. Watts (2006), The long-term strength of continental lithosphere: “Jelly sandwich” or “crème brûlée”?, *GSA Today*, *16*(1), 4.
- Chen, W.-P., and P. Molnar (1983), Focal depths of intracontinental and intraplate earthquakes and their implications for the thermal and mechanical properties of the lithosphere, *J. Geophys. Res.*, *88*(B5), 4183–4214.
- Chew, L. P. (1993), Guaranteed-quality mesh generation for curved surfaces, in *Proceedings of the 9th Annual Symposium on Computational Geometry*, pp. 274–280, ACM, New York, doi:10.1145/160985.161150.
- Connor, C. B., and L. J. Connor (2009), Estimating spatial density with kernel methods, in *Volcanic and Tectonic Hazard Assessment for Nuclear Facilities*, edited by C. Connor, N. Chapman, and L. Connor, pp. 346–368, Cambridge Univ. Press, Cambridge, U. K.
- Connor, C. B., M. Bebbington, and W. Marzocchi (2015), Probabilistic volcanic hazard assessment, in *The Encyclopedia of Volcanoes*, edited by H. Sigurdsson et al., pp. 897–910, Elsevier, Amsterdam.

- Davidson, J., and S. De Silva (2000), Composite volcanoes, in *The Encyclopedia of Volcanoes*, edited by H. Sigurdsson et al., pp. 663–681, Academic Press, San Diego, Calif.
- Davies, D., G. Le Voci, S. Goes, S. Kramer, and C. Wilson (2016), The mantle wedge's transient 3-D flow regime and thermal structure, *Geochem. Geophys. Geosyst.*, *17*, 78–100, doi:10.1002/2015GC006125.
- Desai, C. (1979), *Elementary Finite Element Method, Civil Eng. and Eng. Mech. Ser.*, Prentice Hall, Englewood Cliffs, N. J.
- Desai, C., and T. Kundu (2001), *Introductory Finite Element Method, Mech. and Aeronaut. Eng. Ser.*, Taylor and Francis, Boca Raton, Fla.
- Dixon, J. E., T. H. Dixon, D. Bell, and R. Malservisi (2004), Lateral variation in upper mantle viscosity: Role of water, *Earth Planet. Sci. Lett.*, *222*(2), 451–467.
- El-Fiky, G., and T. Kato (2006), Secular crustal deformation and interplate coupling of the Japanese Islands as deduced from continuous GPS array, 1996–2001, *Tectonophysics*, *422*(1), 1–22.
- Fialko, Y., and J. Pearse (2012), Sombrero uplift above the Altiplano-Puna magma body: Evidence of a ballooning mid-crustal diapir, *Science*, *338*(6104), 250–252.
- Flück, P., R. Hyndman, and C. Lowe (2003), Effective elastic thickness T_e of the lithosphere in western Canada, *J. Geophys. Res.*, *108*(B9), 2430, doi:10.1029/2002JB002201.
- Fung, Y., and P. Tong (2001), *Classical and Computational Solid Mechanics (Advanced Series in Engineering Science)*, vol. 1, World Sci., Singapore.
- Furukawa, Y., and S. Uyeda (1989), Thermal state under the Tohoku Arc with consideration of crustal heat generation, *Tectonophysics*, *164*, 175–187.
- Grocott, J., C. Arévalo, D. Welkner, and A. Cruden (2009), Fault-assisted vertical pluton growth: Coastal Cordillera, north Chilean Andes, *J. Geol. Soc. London*, *166*(2), 295–301.
- Gudmundsson, A. (2006), How local stresses control magma-chamber ruptures, dyke injections, and eruptions in composite volcanoes, *Earth Sci. Rev.*, *79*(1), 1–31.
- Gudmundsson, A. (2011), Deflection of dykes into sills at discontinuities and magma-chamber formation, *Tectonophysics*, *500*(1), 50–64.
- Harayama, S. (1992), Youngest exposed granitoid pluton on Earth: Cooling and rapid uplift of the Pliocene-Quaternary Takidani Granodiorite in the Japan Alps, central Japan, *Geology*, *20*(7), 657–660.
- Hasegawa, A., A. Yamamoto, D. Zhao, S. Hori, and S. Horiuchi (1993), Deep structure of arc volcanoes as inferred from seismic observations, *Philos. Trans. R. Soc. A*, *342*(1663), 167–178.
- Hasegawa, A., J. Nakajima, T. Yanada, N. Uchida, T. Okada, D. Zhao, T. Matsuzawa, and N. Umino (2013), Complex slab structure and arc magmatism beneath the Japanese Islands, *J. Asian Earth Sci.*, *78*, 277–290, doi:10.1016/j.jseas.2012.12.031.
- Hildreth, W. (1981), Gradients in silicic magma chambers: Implications for lithospheric magmatism, *J. Geophys. Res.*, *86*(B11), 10,153–10,192.
- Honda, S., and M. Saito (2003), Small-scale convection under the back-arc occurring in the low viscosity wedge, *Earth Planet. Sci. Lett.*, *216*(4), 703–715.
- Honda, S., T. Gerya, and G. Zhu (2010), A simple three-dimensional model of thermo-chemical convection in the mantle wedge, *Earth Planet. Sci. Lett.*, *290*(3), 311–318.
- Iwasaki, T., V. Levin, A. Nikulin, and T. Iidaka (2013), Constraints on the Moho in Japan and Kamchatka, *Tectonophysics*, *609*, 184–201.
- Jackson, J. (2002), Strength of the continental lithosphere: Time to abandon the jelly sandwich?, *GSA Today*, *12*(9), 4–9.
- Jarvis, A., H. I. Reuter, A. Nelson, and E. Guevara (2008), Hole-filled SRTM for the globe version 4, CGIAR-CSI SRTM 90m Database. [Available at <http://srtm.csi.cgiar.org>.]
- Jellinek, A., C. Johnson, and G. Schubert (2008), Constraints on the elastic thickness, heat flow, and melt production at early Tharsis from topography and magnetic field observations, *J. Geophys. Res.*, *113*, E09004, doi:10.1029/2007JE003005.
- Komazawa, M., et al. (2004), *Gravity CD-ROM of Japan*, Geol. Soc. of Jpn., AIST, Tsukuba, Japan.
- Kondo, H. (2009), Regional-scale volcanology in support of site-specific investigations, in *Volcanic and Tectonic Hazard Assessment for Nuclear Facilities*, edited by C. B. Connor, N. A. Chapman, and L. J. Connor, pp. 307–324, Cambridge Univ. Press, Cambridge, U. K.
- Kruse, S. E., Z. J. Liu, D. F. Naar, and R. A. Duncan (1997), Effective elastic thickness of the lithosphere along the Easter Seamount Chain, *J. Geophys. Res.*, *102*(B12), 27,305–27,317.
- Kulatilake, P. H., J. Park, P. Balasingam, and S. A. Mckenna (2007), Hierarchical probabilistic regionalization of volcanism for Sengan region, Japan, *Geotech. Geol. Eng.*, *25*(1), 79–102.
- Kurasawa, H., I. Imanaga, A. Matsumoto, and K. Shibata (1989), K-Ar age and chemical and strontium isotopic compositions of the Yagura-dake quartz diorite, Ashigara, central Japan, *J. Geol. Soc. Jpn.*, *95*, 331–334.
- Leuthold, J., O. Müntener, L. Baumgartner, and B. Putlitz (2014), Petrological constraints on the recycling of mafic crystal mushes and intrusion of braided sills in the Torres del Paine mafic complex (Patagonia), *J. Petrol.*, *55*(5), 917–949.
- Litchfield, N., Y. Ota, and D. Merritts (2009), Tectonic uplift and subsidence, in *Volcanic and Tectonic Hazard Assessment for Nuclear Facilities*, edited by C. B. Connor, N. A. Chapman, and L. J. Connor, pp. 116–136, Cambridge Univ. Press, Cambridge, U. K.
- Maggi, A., J. Jackson, D. McKenzie, and K. Priestley (2000), Earthquake focal depths, effective elastic thickness and the strength of the continental lithosphere, *Geology*, *28*(6), 495–498.
- Mahony, S., R. Sparks, L. Connor, and C. B. Connor (2009), Exploring long-term hazards using a Quaternary volcano database, in *Volcanic and Tectonic Hazard Assessment for Nuclear Facilities*, edited by C. B. Connor, N. A. Chapman, and L. J. Connor, pp. 326–345, Cambridge Univ. Press, Cambridge, U. K.
- Martin, A. J., K. Umeda, C. B. Connor, J. N. Weller, D. Zhao, and M. Takahashi (2004), Modeling long-term volcanic hazards through Bayesian inference: An example from the Tohoku Volcanic Arc, Japan, *J. Geophys. Res.*, *109*, B10208, doi:10.1029/2004JB003201.
- McTigue, D. (1987), Elastic stress and deformation near a finite spherical magma body: Resolution of the point source paradox, *J. Geophys. Res.*, *92*(B12), 12,931–12,940.
- Meissner, R., and W. Mooney (1998), Weakness of the lower continental crust: A condition for delamination, uplift, and escape, *Tectonophysics*, *296*(1), 47–60.
- Menand, T., C. Annen, and M. De Saint Blanquat (2015), Rates of magma transfer in the crust: Insights into magma reservoir recharge and pluton growth, *Geology*, *43*(3), 199–202.
- Nakano, S., T. Takarada, H. Hoshizumi, J. Itoh, M. Urai, and K. Nishiki (2013), *Quaternary Volcanoes of Japan*, 3rd ed., Geol. Soc. of Jpn., AIST, Tsukuba, Japan. [Available at https://gbank.gsj.jp/volcano/index_e.htm, last modified September 2015.]
- Pearse, J. A., and D. W. Peate (1995), Tectonic implications of the composition of volcanic arc magmas, *Annu. Rev. Earth Planet. Sci.*, *23*, 251–286.
- Pilkington, M., and R. W. Saltus (2009), The Mackenzie River magnetic anomaly, Yukon and Northwest Territories, Canada—Evidence for Early Proterozoic magmatic arc crust at the edge of the North American craton, *Tectonophysics*, *478*(1), 78–86.
- Ruppert, J. (1995), A Delaunay refinement algorithm for quality 2-dimensional mesh generation, *J. Algorithms*, *18*(3), 548–585.

- Rymer, H., and G. Brown (1986), Gravity fields and the interpretation of volcanic structures: Geological discrimination and temporal evolution, *J. Volcanol. Geotherm. Res.*, *27*(3), 229–254.
- Sato, H., K. Muro, and A. Hasegawa (1999), Three-dimensional mapping of magma source and transport regions from seismic data: The mantle wedge beneath northeastern Japan, in *Q of the Earth: Global, Regional, and Laboratory Studies*, edited by B. J. Mitchell and B. Romanowicz, pp. 377–398, Springer, Basel, Switzerland.
- Schurr, B., G. Asch, A. Rietbrock, R. Trumbull, and C. Haberland (2003), Complex patterns of fluid and melt transport in the central Andean subduction zone revealed by attenuation tomography, *Earth Planet. Sci. Lett.*, *215*(1), 105–119.
- Shewchuk, J. R. (1996), Triangle: Engineering a 2D quality mesh generator and Delaunay triangulator, in *Applied Computational Geometry Towards Geometric Engineering*, edited by M. C. Lin and D. Manocha, pp. 203–222, Springer, Berlin.
- Shewchuk, J. R. (2002), Delaunay refinement algorithms for triangular mesh generation, *Comput. Geom.*, *22*(1), 21–74.
- Singh, B., M. P. Rao, S. Prajapati, and C. Swarnapriya (2014), Combined gravity and magnetic modeling over Pavagadh and Phenaimata igneous complexes, Gujarat, India: Inference on emplacement history of Deccan volcanism, *J. Asian Earth Sci.*, *80*, 119–133.
- Solano, J., M. Jackson, R. Sparks, J. Blundy, and C. Annen (2012), Melt segregation in deep crustal hot zones: A mechanism for chemical differentiation, crustal assimilation and the formation of evolved magmas, *J. Petrol.*, *53*, 1999–2026.
- Sparks, R., C. Folkes, M. Humphreys, D. Barfod, J. Clavero, M. Suagua, S. McNutt, and M. Pritchard (2008), Uturuncu Volcano, Bolivia: Volcanic unrest due to mid-crustal magma intrusion, *Am. J. Sci.*, *308*(6), 727–769.
- Tamura, Y., Y. Tatsumi, Z. Dapeng, Y. Kido, and H. Shukuno (2001), Distribution of Quaternary volcanoes in the Northeast Japan arc: Geological and geophysical evidence of hot fingers in the mantle wedge, *Proc. Jpn. Acad. B*, *77*(7), 135–139.
- Tamura, Y., Y. Tatsumi, D. Zhao, Y. Kido, and H. Shukuno (2002), Hot fingers in the mantle wedge: New insights into magma genesis in subduction zones, *Earth Planet. Sci. Lett.*, *197*(1), 105–116.
- Tesaro, M., M. K. Kaban, and S. A. P. L. Cloetingh (2013), Global model for the lithospheric strength and effective elastic thickness, *Tectonophysics*, *602*, 78–86, doi:10.1016/j.tecto.2013.01.006.
- Thouret, J.-C. (1999), Volcanic geomorphology—An overview, *Earth Sci. Rev.*, *47*(1), 95–131.
- Timoshenko, S., and J. Goodier (1951), *Theory of Elasticity*, 2nd ed., 506 pp., McGraw-Hill, New York.
- Tiwari, V., M. V. Rao, D. Mishra, and B. Singh (2006), Crustal structure across Sikkim, NE Himalaya from new gravity and magnetic data, *Earth Planet. Sci. Lett.*, *247*(1), 61–69.
- Tizzani, P., M. Battaglia, G. Zeni, S. Atzori, P. Berardino, and R. Lanari (2009), Uplift and magma intrusion at Long Valley caldera from InSAR and gravity measurements, *Geology*, *37*(1), 63–66.
- Ueki, K., and H. Iwamori (2007), Melting condition and origin of arc magmas beneath the Sengan region, Northeastern Japan, *Geochim. Cosmochim. Acta*, *71*, A1045.
- Walker, G. P. (1989), Gravitational (density) controls on volcanism, magma chambers and intrusions, *Aust. J. Earth Sci.*, *36*(2), 149–165.
- Wallace, M. H., and H. J. Melosh (1994), Buckling of a pervasively faulted lithosphere, *Pure Appl. Geophys.*, *142*(2), 239–261.
- Wang, Z., and D. Zhao (2005), Seismic imaging of the entire arc of Tohoku and Hokkaido in Japan using *P*-wave, *S*-wave and *sP* depth-phase data, *Phys. Earth Planet. Inter.*, *152*(3), 144–162, doi:10.1016/j.pepi.2005.06.010.
- Watts, A. (2001), *Isostatic Response Functions, Isostasy and Flexure of the Lithosphere*, pp. 180–192, Cambridge Univ. Press, New York.
- Williams, C. A., and R. M. Richardson (1991), A rheologically layered three-dimensional model of the San Andreas Fault in central and southern California, *J. Geophys. Res.*, *96*(B10), 16,597–16,623.
- Xia, S., D. Zhao, X. Qiu, J. Nakajima, T. Matsuzawa, and A. Hasegawa (2007), Mapping the crustal structure under active volcanoes in central Tohoku, Japan using *P* and *PmP* data, *Geophys. Res. Lett.*, *34*, L10309, doi:10.1029/2007GL030026.
- Zandt, G., H. Gilbert, T. Owens, M. Ducea, J. Saleeby, and C. Jones (2004), Active foundering of a continental arc root beneath the southern Sierra Nevada in California, *Nature*, *431*(7004), 41–46.
- Zhao, D., S. Horiuchi, and A. Hasegawa (1990), 3D seismic velocity structure of the crust and the uppermost mantle in the northeastern Japan Arc, *Tectonophysics*, *181*(1), 135–149.
- Zhao, D., A. Hasegawa, and S. Horiuchi (1992), Tomographic imaging of *P* and *S* wave velocity structure beneath northeastern Japan, *J. Geophys. Res.*, *97*(B13), 19,909–19,928.
- Zhao, D., A. Hasegawa, and H. Kanamori (1994), Deep structure of Japan subduction zone as derived from local, regional, and teleseismic events, *J. Geophys. Res.*, *99*(B11), 22,313–22,329.
- Zhao, D., F. Ochi, A. Hasegawa, and A. Yamamoto (2000), Evidence for the location and cause of large crustal earthquakes in Japan, *J. Geophys. Res.*, *105*(B6), 13,579–13,594.